Targeting Multiple Conformations Leads to Small Molecule Inhibitors of the uPAR·uPA Protein-Protein Interaction that Block Cancer Cell Invasion

May Khanna[1], **Fang Wang**[1], **Inha Jo**[1], **W. Eric Knabe**[1], **Sarah M. Wilson**[4], **Liwei Li**[1,3], **Khuchtumur Bum-Erdene**[1,3,8], **Jing Li**[1], **George Sledge**[6], **Rajesh Khanna**[2,4], and **Samy O. Meroueh**[1,3,4,5,8]

Samy O. Meroueh: smeroueh@iupui.edu

[1]Department of Biochemistry and Molecular Biology, Indiana University School of Medicine, Indianapolis, IN 46202

[2]Department of Pharmacology and Toxicology, Indiana University School of Medicine, Indianapolis, IN 46202

[3]Center for Computational Biology and Bioinformatics, Indiana University School of Medicine, Indianapolis, IN 46202

[4]Stark Neuroscience Research Institute, Indiana University School of Medicine, Indianapolis, IN 46202

[5]Indiana University Cancer Center, Indiana University School of Medicine, Indianapolis, IN 46202

[6]Department of Medicine, Indiana University School of Medicine, Indianapolis, IN 46202

[7]Medical Neuroscience Program, Indiana University School of Medicine, Indianapolis, IN 46202

[8]Department of Chemistry and Chemical Biology, Indiana University Purdue University Indianapolis (IUPUI), Indianapolis, Indiana, 46202

Abstract

Interaction of the urokinase receptor (uPAR) with its binding partners including the urokinase-type plasminogen activator (uPA) at the cell surface triggers a series of proteolytic and signaling events that promote invasion and metastasis. Here, we report the discovery of a small molecule (IPR-456) and its derivatives that inhibit the tight uPAR·uPA protein-protein interaction. IPR-456 was discovered by virtual screening against multiple conformations of uPAR sampled from explicit-solvent molecular dynamics simulations. Biochemical characterization reveal that the compound binds to uPAR with sub-micromolar affinity (K_d = 310 nM) and inhibits the tight protein-protein interaction with an IC_{50} of 10 μM. Free energy calculations based on explicit-solvent molecular dynamics simulations suggested the importance of a carboxylate moiety on IPR-456, which was confirmed by the activity of several derivatives including IPR-803. Immunofluorescence imaging showed that IPR-456 inhibited uPA binding to uPAR of breast MDA-MB-231 tumor cells with an IC_{50} of 8 μM. The compounds blocked MDA-MB-231 cell invasion, but IPR-456 showed little effect on MDA-MB-231 migration, and no effect on adhesion, suggesting that uPAR mediates these processes through its other binding partners.

Keywords

Virtual screening; small molecule; protein-protein interaction; inhibitor; urokinase receptor; invasion; migration; metastasis; MDA-MB-231; cancer; breast cancer; urokinase-type plasminogen activator; uPAR; uPA; docking; scoring; flexible docking

INTRODUCTION

The interaction of the glycosylphosphatidylinositol (GPI)-anchored cell-surface urokinase receptor (uPAR) with its serine protease ligand urokinase-type plasminogen activator (uPA), has been implicated in nearly every step of tumor formation and progression, including tumorigenesis (1), cell proliferation (2–4), cell migration (5, 6), adhesion (3, 7), angiogenesis (8, 9), and invasion (3, 4, 10, 11). The uPAR·uPA complex formation enhances pericellular proteolysis through activation of plasminogen (7), culminating in the active degradation of extracellular matrix (ECM) components. Whereas uPAR has no inherent signaling capability, a large body of evidence has shown that the uPAR·uPA complex promotes signaling by actively associating to cell surface receptors such as integrins (12), receptor tyrosine kinases (RTKs) (13, 14), and G-protein coupled receptors (GPCRs) (15). Furthermore, uPAR binding to vitronectin components indicates interactions that extend beyond the cell surface to engage the microenvironment and further promotes metastasis.

To date, while peptides and antibodies have been reported to inhibit the uPAR·uPA complex (16), there is not a single small organic molecule that inhibits the tight sub-nanomolar uPAR·uPA interaction. Moreover, most efforts have concentrated on inhibiting the enzymatic activity of uPA, neglecting the signaling capabilities of the receptor. The uPAR·uPA complex (Fig. 1a) poses the same challenges that have plagued prior efforts to inhibit protein-protein interactions with small molecules (17), due to the tightness of the protein-protein interaction (18, 19), the large interaction surface which is estimated at 1,318 $\mathring{A}^2$ (20), and the inherent flexibility of the target (Fig. 1b) (21). Despite initial pessimism, several successes in the past decade have demonstrated that small molecules can inhibit protein-protein interactions (22–27). These successes have benefitted from our increased understanding of the forces that drive protein-protein interactions (28). In particular, it is known that the strength of a protein-protein interaction is not evenly spread across the large interface, but is concentrated in a few residues known as 'hot-spots' that preferentially contribute nearly an order or magnitude or more to the binding (23, 26). Protein-protein interactions can be categorized as either tight or transient (28), and inhibitors of tight interactions such as uPAR·uPA remain scarce (21). The only example of small molecules that inhibit a protein interaction with similar potency as the uPAR·uPA interaction are inhibitors of the Bcl-2 family reported by Abbott laboratories (24, 29). Despite the importance of protein-protein interactions in biological processes, structure-based design approaches, including those that consider receptor flexibility (30), have yet to be extensively applied in the rational design of protein-protein interaction inhibitors. The primary challenge is to distinguish between molecules that merely bind to a target, which is routinely achieved, with molecules that are capable of displacing the full protein-protein interaction.

Here, we follow a rational approach to the search for small molecules that inhibit the uPAR·uPA interaction. We target alternative conformations of uPAR at a binding cavity that is rich in hot-spot residues. Representative conformers were collected from molecular dynamics (MD) simulations and were then targeted by docking 10,000 compounds (that emerged from an initial library of 5 million). The highest scoring 50 compounds were selected and assessed for activity with a fluorescence polarization assay and a microtiter-based ELISA that we developed. A series of derivative compounds that were tested with

ELISA and surface plasmon resonance (SPR) provided valuable insight into the key groups required for activity. Immunofluorescence imaging in breast (MDA-MB-231) tumor cells was performed to confirm that IPR-456 inhibited uPA binding to uPAR at the cell surface. Finally, the compounds were evaluated for their ability to block processes critical to metastasis, such as invasion, migration and adhesion of MDA-MB-231 tumor cells. The results provided valuable biological insights into the role the uPAR·uPA interaction in these processes.

METHODS

Protein Purification

The soluble fraction of uPAR comprising amino acids 1–277 was expressed in Drosophila S2 cells and purified by a peptide column as previously described (31). The purified protein was analyzed with SDS-PAGE gel and found to be greater than 95% purity. The protein was determined to be functional based on a fluorescence polarization (FP) assay developed in our laboratory (discussed below), as well as binding to immobilized uPA using surface plasmon resonance (SPR). The soluble fraction of uPA (scuPA) and uPA$_{ATF}$ (amino terminal fraction of uPA) were purified by an anion exchange column (SP Sepharose). This was followed by a second step of purification with a reverse phase-HPLC using a C$_8$ column where the protein is eluted with an increasing gradient of acetonitrile over 1 hour as described previously.

Cell Culture

MDA-MB-231 cells were cultured in Dulbecco's Modified Eagle Medium (Cellgro, Manassas, VA). Each medium was supplemented with 10% FBS and 1% penicillin/streptomycin in a 5% CO$_2$ atmosphere at 37°C.

Reagents

Mouse anti–human uPAR antibody 3937 and rabbit anti-human uPA antibody 389 were purchased from America Diagnostica (Stanfford, CT). Biotinylated anti-human uPAR antibody was purchased from R&D Systemsn (Minneapolis, MN). uPAR siRNA and control siRNA were purchased from Santa Cruz Biotechnology (Santa Cruz, CA).

Invasion Assay

The undersurface of the inserts (was coated with 30 ng μl^{-1} of fibronectin at 4 °C overnight. Invasion transwell chambers were purchased from BD bioscience (San Jose, CA) (32). The filters were equilibrated with 0.5 mL of serum-free medium for 2 h. After 4 h of serum starvation, cells were harvested and 5×10^4 cells in 500 μl medium containing 0.1% FBS and the indicated compounds were plated onto the upper chamber of a transwell filter. 500 μL of 10% FBS medium containing compounds or DMSO control was added to the lower chamber. After a 16 h incubation at 37°C in 5% CO$_2$, the filters were fixed and the number of cells that had invaded was determined as described in the migration assay.

Transwell Migration Assay

24-well transwell plates (Costar, Corning, NY) were coated with 30 ng μL^{-1} of fibronectin at 4°C overnight. After 4 h of serum starvation, 5×10^4 cells in 250 μL of 0.1% FBS medium containing the same amount of compounds or DMSO were added to the upper chamber and incubated at 37 °C for 8 h. 500 μL of 10% FBS RPMI-1640 medium containing compounds or 1% DMSO control was added to the lower chamber Non-invaded cells on the top of the transwell were scrapped off with a cotton swab, and the cells that migrated through the filter were fixed in methanol for 30 min and stained with Hematoxylin

Stain (Fisher, SH30-500D) for 1 h. The number of migrated cells was counted in ten separate $200 \times$ fields and averaged across three independent experiments. Cytotoxicity of the compounds on the cells was measured at the same concentrations used in the migration assay and using the same incubation time, save for the addition of MTT (3-(4,5-dimethylthiazol-2-yl)-2,5-diphenyltetrazolium bromide) 2h before measurement.

Wound Healing Assay

Confluent cell monolayers in 12-well plates were wounded by scraping with a micropipette tip. The cells were washed and then cultured in complete media containing the compounds. The degree of wound closure was assessed in three randomly chosen regions by measuring under Nikon Diaphot 300 microscope the distance between the wound edges just after wounding and after 16 h.

Adhesion Assay

96-well plates were coated with 15ng μl^{-1} fibronectin (Sigma, St. Louis, Missouri) at 4°C overnight, then blocked with 0.5% BSA in PBS for 1 h. After starving with serum-free medium for 3h, MDAMB231 cells (2.5×10^5 cells ml^{-1}) were trypsinized and suspended in 100 μl of 0.1% FBS DMEM medium with various concentrations of uPAR compounds or DMSO control at 37°C for 90 min. Medium was then carefully suctioned out from each well. Each well was washed three times with PBS. MTT-assay was used to determine the number of remaining cells (adherent cells).

siRNA Knockdown and Western Blot Analysis

MDA-MB-231 cells incubated for 48 hrs. Cells were then collected, and total cell lysates were prepared in standard RIPA extraction buffer containing aprotinin and phenyl-methyl-sulfonyl-fluoride. Twenty μg of protein from these samples was separated by 12% SDS-PAGE and transferred to nitrocellulose membranes (Amersham, Arlington Heights, IL). The membranes were immunoprobed with antibodies against biotin-uPAR at 4°C overnight. Next, membranes were treated with the appropriate HRP-conjugated secondary antibody and then developed according to enhanced chemiluminescence protocol (Thermo Scientific, Rockford, IL). Membranes were stripped and reprobed with a monoclonal antibody against actin as a loading control.

Virtual Screening and Free Energy Calculations

Two uPAR crystal structures (PDB ID: 1YWH and 2FD6) were imported into SYBYL 8.0, a molecular modeling suite from Tripos Inc., for pre-docking preparation. All binding partners, counterions and water molecules were removed. Missing gaps were modeled using BIOPOLYMER module in SYBYL. Hydrogen atoms were added and protonation states were optimized with *Reduce* (vers 3.03) program (33). Structures were then loaded into AutoDockTools (34). Gasteiger charges were assigned. Non-polar hydrogen atoms were merged. A binding box with side length of 15 Å was defined to encompass the uPA binding site. Autodock4 (35) was employed to dock compounds to the crystal structures. Default docking parameters were used. In total, nearly 5 million compounds from six vendors (ChemDiv, ChemBridge, Enamine, Aurora, IBScreen) listed on the ZINC Web site (36) were screened on the Indiana University Big Red supercomputer. Post-docking analysis was performed to score the docked complexes. A set of scoring functions, including ChemScore, GoldScore, PMF, Autodock4, X-score, DFIRE, and consensus scoring function, were employed to score the docked complexes. Compounds were ranked based on the score they received. The 2,000 most favorable compounds predicted by each scoring function were combined to give ~10,000 compounds pertaining to each crystal structure, which were further screened using multiple conformer strategy. Blind docking was performed with the

AutoDock4 docking program following a similar procedure used for the virtual screening, except that the binding box encompassed the entire protein rather than just the uPA binding pocket.

Explicit solvent MD simulations sampled the uPAR conformations in solution. To perform MD simulations, crystal structures prepared with SYBYL were solvated with TIP3P (37) water molecules and were further neutralized with Na^+ or Cl^- counter ions using *Leap* program from the AMBER9 package (38). Water molecules from the crystal structures were retained in this process. An annealing process (39) equilibrated the solvated structures before production runs were carried out using *pmemd* in AMBER. MD snapshots were saved every 2 ps, yielding 5,000 structures per trajectory. By assigning different initial velocities, five independent trajectories of 10 ns in length were collected for each of the crystal structures. Structures from MD were clustered using only the heavy atoms of the uPA binding site using *ptraj* program in AMBER. A total of 50 conformers (25 each from 1YWH and 2FD6) and exhibiting distinct pocket structures were selected. The top compounds (~10,000) from the virtual screening were docked into each of the 50 structures with AutoDock4. The docked complexes were scored and the top 250 compounds were selected using ChemScore and GoldScore (500 total). These 500 compounds were docked onto their corresponding conformer using Glide (Glide, version 5.5, Schrödinger, LLC, New York, NY) resulting in $50 \times 500 = 25,000$ complexes. The default parameters for flexible ligand docking protocol in Glide SP were used to rank 25,000 complexes. The top 500 compounds were clustered by similarity and the highest scoring compound from each of the top 50 clusters was selected for *in vitro* testing.

The binding energy of both these compounds and the peptide (*vide infra*) for uPAR protein was calculated with MM-PBSA/GBSA approach (40) following multi-trajectory MD simulation of the complexes, using a setup similar to those of uPAR in its apo, as reported above. The compound conformation on uPAR was provided from docking results while the peptide bound conformation was extracted from PDB structure (PDB ID: 3BT1). AM1-BCC (41) charges were assigned to compounds by the *antechamber* program in the AMBER9 package. For each complex, 6 independent simulations (8 ns each) were carried out after annealing runs. The first ~3 ns of each trajectory was excluded from binding energy calculations. In total, 600 snapshots were extracted at regular intervals from the production trajectories and subjected to MM-PBSA/GBSA free energy analysis. The MM-PBSA Perl script in AMBER9 was used for the binding energy components calculations and to decompose the binding energy on a per residue basis (42). The latter provided useful insight on the relative importance of residues on the pocket to the binding of ligand to uPAR.

Compounds

The 50 compounds that emerged from virtual screening were purchased from ChemDiv (11 compounds), ChemBridge (9 compounds), Asinex (3 compounds), Enamine (20 compounds), and Princeton Biomolecular Research (7 compounds). All IPR-456 derivatives were acquired from ChemDiv. The stipulated purity of the compounds by the vendor was greater than 90% pure (>95% typical by analysis). Compounds were maintained as DMSO stock solution. Mass spectrometry and ^{1}H and ^{13}C NMR confirmed purity and also the structures of IPR-456 and IPR-803. The ^{1}H spectra show the characteristic resonance for the intramolecularly hydrogen-bonded NH (to the adjacent carbonyl) at δ 11.79 and for the 4-CH methine at δ 6.12, consistent with literature values (43):

2-((3-(3,5-Dimethylpiperidin-1-yl)-6-oxo-6H-anthra[1,9-cd]isoxazol-5-yl)amino)benzoic acid (IPR-456)—^{1}HNMR (500 MHz, DMSO) δ 12.2 (s, 1H), 8.45 (d, J = 8 Hz, 1H), 8.16 (d, J = 7.5 Hz, 1H), 8.00 (d, J = 8 Hz, 1H), 7.88–7.78 (m, 2H), 7.75–7.62

(m, 2H), 7.32 (t, J = 7.5 Hz, 1H), 6.41 (s, 1H), 4.52–4.37 (br s, 1H), 2.78 (t, J = 12 Hz, 2H), 1.86–1.69 (m, 3H), 0.95–0.86 (m, 6H); ^{13}C NMR (126 MHz, DMSO) δ 175.2, 167.2, 154.1, 151.4, 148.2, 145.0, 139.0, 133.1, 132.8, 131.7, 128.6, 127.7, 124.6, 124.0, 123.7, 123.2, 121.9, 118.9, 99.5, 96.5, 95.8, 55.9, 41.5, 30.9, 18.8.

3-((3-(Azepan-1-yl)-6-oxo-6H-anthra[1,9-cd]isoxazol-5-yl)amino)benzoic acid (IPR-803)—^{1}H NMR (500 MHz, DMSO) δ 11.79 (s, 1H), 8.44 (app d, J = 8 Hz, 1H), 8.13 (app d, J = 8 Hz, 1H), 8.01 (s, 1H), 7.84–7.78 (m, 2H), 7.72–7.67 (m, 2H), 7.64–7.59 (m, 1H), 6.12 (s, 1H), 4.51–3.97 (br s, 3H), 1.80 (br s, 4H), 1.55 (br s, 4H); ^{13}C NMR (126 MHz, DMSO) δ 174.7, 166.8, 153.6, 152.8, 147.6, 146.0, 138.5, 132.9, 132.4, 131.2, 130.2, 128.3, 127.5, 127.4, 126.0, 123.4, 121.8, 118.5, 99.5, 95.0, 91.7, 56.0, 26.0, 18.6.

Microtiter-Based ELISA

Medium to high-binding microplates were coated and incubated for 1 h at 4°C with 100 μL of 2 μg mL^{-1} of uPA$_{ATF}$ in 1xPBS for immobilization. A 1:1 mixture of Superblock® buffer in PBS (Thermo Fisher Scientific, Inc.) with 0.04 M NaH$_2$PO$_4$ and 0.3 M NaCl buffer was used for blocking. Following incubation and washing steps, uPA1310 biotinylated antibody (R&D Systems) in 1% BSA 1x PBS buffer was added to the wells (100 μL/well) and incubated for 1–2 h to allow for the detection of bound uPAR. The signal obtained in the presence of streptavidin-peroxidase and hydrogen peroxide was detected using an EnVision® Multilabel Plate Readers (PerkinElmer).

Immunofluorescence Imaging

Immunocytochemsitry was performed as described previously (44). MDA-MB-231 cells were grown on laminin-coated glass coverslips, exposed to 100 μM of IPR-456 for 30 min at 37 °C, washed with PBS, fixed with 4% paraformaldehyde for 20 min, and permeabilized with 1% Triton X-100 for 10 min. Non-specific binding was blocked with 5% normal goat serum, 5% BSA, 0.01% Triton X-100 in PBS at RT for 1 h. The cells were then incubated overnight at 4 °C with rabbit polyclonal anti-human uPA or mouse monoclonal anti-human uPAR antibodies (both at a dilution of 1:100 in 1% BSA/PBS). After three-fold washing with PBS, the cells were incubated with anti-rabbit IgG conjugated with Alexa 594 Texas Red (Invitrogen Corporation) or goat anti-mouse IgG conjugated with Alexa Fluor 488 (Invitrogen Corporation), both at a dilution of 1:1000 in 1% BSA/PBS at RT for 1 h in the dark. Images were acquired using a Nikon swept-filed confocal microscope.

Fluorescence Polarization (FP) Assay

Inhibitor screens were carried out in triplicate using 500 nM uPAR, 50 nM of a fluorescein-labeled peptide (GFD-FAM, ; synthesized by Antagene, Inc., California) and inhibitor concentrations ranging from 0.78 μM to 100 μM in 50 μL volumes in black BD Falcon 384-well microplates. The compounds were serially diluted in DMSO then diluted in to 0.01% Triton X-100 in 1x PBS buffer ensuring a final concentration of 2% DMSO (a concentration that did not affect peptide binding to uPAR). Polarized fluorescence intensities were measured immediately following addition of inhibitors to the protein-peptide mix at room temperature on an EnVision® Multilabel Plate Readers (PerkinElmer) using excitation and emission wavelengths of 485 and 530 nm, respectively. For direct binding studies of IPR-456 using FP, we used an excitation of 530 nm and emission of 600 nm. FP of IPR-456 in the presence and absence of protein was measured using identical conditions as described above. Inhibition constants were measured using the K_i calculator available at the following site: http://sw16.im.med.umich.edu/software/calc_ki.

Surface Plasmon Resonance (SPR)

A Biacore 3000 instrument (GE Healthcare Life Sciences) was used to detect competitive inhibition of binding between suPAR277 and the amino terminal fragment of uPA (uPA_{ATF}) in the presence of small molecule inhibitors. uPA_{ATF} was immobilized on a CM-5 sensor chip (Biacore) using amine coupling chemistry recommended by the manufacturer. Surface densities of 100 RU were used for competitive screening of uPA_{ATF} to suPAR. The running buffer was HBS-EP was obtained from GE (GE healthcare Bio-sciences). For the injection of inhibitors that included DMSO, the buffer was supplemented with 5% DMSO. Protein controls, which included DMSO but no inhibitor, were injected after two to three injections with inhibitors to ensure that neither regeneration nor the inhibitors affected the immobilized uPA_{ATF}. All samples were prepared from 10 mM stock solutions to final concentrations ranging from 5 to 100 μM in 5% DMSO. Injections of suPAR (60 μL) in the presence and absence of inhibitors were done at 20 μL min^{-1} with 180 s association and 90 s dissociation time. Regeneration used a single injection of 10 μL of 5 mM HCl. Identical injections and regenerations were used to obtain the K_d of binding of uPAR to uPA_{ATF}. Varying concentrations of suPAR ranging from 0.9 nM to 2 μM to were injected onto the immobilized uPA_{ATF}.

RESULTS

Computational Search of Chemical Databases

A total of 80,000 structures from explicit-solvent MD simulations of uPAR were distilled into a representative set of 50 conformations (Fig. 1c). This was accomplished by clustering the conformers by root-mean-square (r.m.s.) deviation using residues located within the growth factor-like domain (GFD) binding cavity on uPAR (Fig. 1b). Comparison of the overall structure of these conformers using r.m.s. deviation of backbone atoms with those of the crystal structure of uPAR (PDB code: 1YWH) revealed significant differences. Overall the r.m.s. derivation ranged from 1.5 to 7 Å. These MD simulations provided the structures used for virtual screening. Docking was focused at the GFD binding site (orange surface in Fig 1b) of uPA, as it contains the majority of hot-spot residues (19). The multi-tiered virtual screening approach consisted of first docking 5 million compounds from five commercial databases to two existing uPAR crystal structures (PDB ID: 2FD6 and 1YWH). The resulting complexes were scored with the Gold and ChemScore scoring functions. The top 10,000 compounds were selected (2,000 for each scoring function). These were docked to each of the 50 conformations that emerged from MD with AutoDock4 and scored with Gold and ChemScore. The top scoring 500 compounds were re-docked onto their corresponding structure with Glide resulting in $500 \times 50 = 25,000$ complexes. These complexes were scored with Glide, and the top 250 compounds were clustered by chemical similarity. A representative compound from each of the top 50 clusters was selected and purchased from five different vendors.

Fluorescence Polarization Screening Identifies Active Compounds

To identify the compounds among the top 50 virtual screening candidates that bind to uPAR at its interface with uPA, we developed a fluorescent polarization assay using a probe with a fluorescein label at the N-terminus of GFD (GFD-FAM). GFD-FAM binds strongly to uPAR with a dissociation constant (K_D) of 120 nM (Fig. 2a). All 50 compounds that emerged from the computational screening were tested initially at a single concentration of 50 μM in this assay. Four compounds, IPR-455, IPR-456, IPR-566 and IPR-593 showed the highest inhibition (Fig. 2b). To confirm these results, IPR-456, IPR-566 and IPR-593 were shown to displace GFD-FAM in a concentration-dependent manner (Fig. 2c). As expected, unlabeled GFD peptide also displaced GFD-FAM in a concentration dependent manner with an inhibition equilibrium constant $K_i = 220$ nM (Fig. 2c). IPR-455 did not show any

inhibition and is considered a false-positive. IPR-456 exhibited a K_i value of 140 nM. IPR-593 did not completely displace GFD-FAM as evidenced by an asymptotic curve that reached a plateau at 60%. IPR-566 also inhibited GFD-FAM binding with a K_i = 4.9 μM

IPR-456 Inhibits uPAR·uPA Binding

Given that GFD-FAM only occupies a fraction of the total contact surface between uPAR and uPA, we sought to establish that compounds that displaced GFD-FAM also abrogate the full uPAR·uPA interaction. To this end, we developed a microtiter-based ELISA using uPAR and the amino-terminal fragment (uPA$_{ATF}$), which includes the entire binding surface of full-length uPA (20). IPR-456, IPR-566 and IPR-593 were tested at multiple concentrations for inhibition of uPAR binding to uPA using this ELISA. As shown in Fig. 2d, only IPR-456 and GFD showed complete concentration-dependent inhibition of uPA$_{ATF}$ binding to uPAR with an IC$_{50}$ of 10 μM. Some of the difference between the ELISA and FP IC$_{50}$ of IPR-456 can be attributed to the fact that the peptide used in the FP assay does not contain the entire binding surface and is therefore more easily displaced than the uPA$_{ATF}$. IPR-566 and IPR-593 did not inhibit uPAR binding to uPA in this ELISA. As described below, it is likely that these compounds did not engage sufficient hot-spot residues and showed weaker binding to individual side chains within the binding site.

Probing Direct Binding of IPR-456 to uPAR

We exploited the inherent red-colored fluorescence of IPR-456 to probe its direct binding to uPAR using fluorescence polarization. As shown in Fig. 2e, increasing the concentration of uPAR led to a corresponding increase in the fluorescence polarization, confirming direct binding between IPR-456 to uPAR with a K_d of 310 nM. When the study was repeated in the presence 10 μM GFD, no increase in the polarization was detected with increasing concentration of uPAR (Fig. 2e), suggesting that GFD blocked IPR-456 binding to uPAR. These results further establish that IPR-456 competes against GFD likely for the same site on uPAR. Hence, the fact that IPR-456 binds directly to uPAR argues against non-specific inhibition, such as may be observed as a result of protein aggregation (45). Additional evidence that argues against non-stoichiometric binding due to aggregation include (i) the high level of binding of IPR-456 to uPAR as shown in Fig. 2e even at sub-μM concentrations; (ii) strong binding as well as inhibition even in the presence of detergent (0.01 % Triton X-100) (Fig. 2c); and (iii) the lack of steepness in the inhibition (Fig. 2c) and binding curves (Fig. 2e).

MD Simulation and Free Energy Calculations Support Important Role of Carboxylate with Arg53

To gain insight into the binding mechanism of IPR-456, we resorted to intensive explicit-solvent molecular dynamics simulations complemented by free energy calculations following the widely used MM-GBSA approach as we have used previously (46–48). Docking IPR-456 on the entire surface of uPAR showed that 83 out of the 95 runs resulted in a complex with IPR-456 bound to the uPA binding pocket. This blind docking approach provides additional evidence that IPR-456 binds to the uPA binding pocket on uPAR.

Further insight into the basis for IPR-456's binding strength can be gained from determining the energetic contribution of each amino acid in the binding pocket of uPAR that come in contact with IPR-456. Toward this end, we performed residue-based free energy calculations (ΔE_{RES}). Calculations consisted of computing the energy of interaction between each of these residues and IPR-456. The components of the free energy of binding are: (i) a non-polar component ($\Delta E_{NP} = \Delta E_{VDW} + \Delta E_{SA}$), which comprises the sum of the van der Waals potential energy and non-polar solvation energy; (ii) a polar component ($\Delta E_{ELE} = \Delta E_{COUL} + \Delta E_{GB}$), which consists of the Coulomb electrostatic energy and the Generalized-Born

solvation energy (Table 1). Each residue was color-coded based on its contribution to uPA binding as determined from a recent comprehensive alanine scanning study using SPR (49). During the simulations, IPR-456 engaged more residues on the receptor, coming in contact with a total of 7 amino acids, compared with 6 and 5 for IPR-593 and IPR-566, respectively. Also, IPR-456's interaction with hot-spot residues was stronger. For example, the binding energy to Leu150 is -2.7 kcal·mol^{-1} for IPR-456, compared to -2 kcal·mol^{-1} for IPR-593 and -1.7 kcal·mol^{-1} for GFD. Another interesting observation is that the sum of the individual interaction energies across all the amino acids that come into contact with each compound is significantly greater in IPR-456 (-14.6 kcal·mol^{-1}) compared with IPR-566 (-7.0 kcal·mol^{-1}) and IPR-593 (-9.5 kcal·mol^{-1}).

Finally, we note that IPR-456 makes the strongest interaction with Arg53 (-5.3 kcal·mol^{-1}), which is also found to be the residue that most strongly interacts with GFD (-2.4 kcal·mol^{-1}). Analysis of the MD simulation data of IPR-456 in complex with uPAR reveals that the compound forms a hydrogen bond with Arg53 through its carboxylate group, likely a salt-bridge interaction. IPR-566 does not appear to bind to Arg53, while IPR-593 shows a weaker interaction (-1.6 kcal·mol^{-1}) compared with IPR-456 and GFD.

Derivatives of IPR-456 Confirm Critical Role of Carboxylate

The effect of structural modification around the IPR-456 structure was evaluated using a set of 8 derivatives of IPR-456 (Scheme 2). IPR-631 and IPR-831, which share the same core structure as IPR-456, showed minimal activity in the ELISA (Fig. 3a). This lack of activity was attributed to the loss of the benzoic acid moiety of IPR-456 (replaced with a methyl group in IPR-631, and by an indoline ring in IPR-831). Only the three compounds that possessed a benzoic acid moiety (IPR-659, IPR-803, and IPR-808) consistently showed strong activity. Interestingly, the precise position of the carboxylic acid on the benzoic acid moiety did not strongly impact affinity. Compounds with a meta-carboxylate (IPR-659 and IPR-803) and para-carboxylate (IPR-808) show slightly better activity than the ortho-carboxylate (IPR-456). The presence of the negatively charged carboxylate appears more important than its position on the phenyl substituent. Indeed, loss of this negative charge by esterification (IPR-805, a methyl ester) gave complete loss of activity. The strong activity of IPR-763 suggests that the aromatic ring of the benzoic acid moiety is not critical for activity, since its replacement with a propionic acid did not abrogate inhibition. The complete loss of activity observed for IPR-792 further confirms the critical nature of the charge provided by the carboxylic acid moiety to the binding energies of IPR-456 and its derivatives.

Four IPR-456 derivatives (IPR-763, IPR-803, IPR-805, and IPR-808) were selected for a concentration-dependent study. A compound that is not an analog of IPR-456 and showed no activity in the initial screen (IPR-519) was also included to rule out non-specific effects that may be due simply to the presence of a carboxylate. Consistent with our expectation, IPR-763, IPR-803 and IPR-808 all demonstrated a concentration-dependent inhibition, with IPR-803 exhibiting the highest affinity (Fig. 3b) with IC$_{50}$ values of 20, 10, and 30 μM, respectively (Fig. 3b). Neither IPR-519 nor IPR-805 showed any inhibition, consistent with the initial data obtained at single concentration.

SPR experiments evaluated the effect of these compounds on the uPAR·uPA protein-protein interaction. One binding partners (the ligand) is covalently attached to the biosensor chip on a dextran surface while the other (the analyte) flows over the ligand. In the event of binding, an increase in the sensorgram signal is observed (50). We immobilized uPA$_{ATF}$ on the CM5 chip dextran surface and injected uPAR along with increasing concentration of IPR-763 and IPR-803. As shown in Fig. 3c, a concentration-dependent decrease in the response is detected for each compound. Moreover, the IC$_{50}$ estimated from the plots were nearly identical to those observed in the ELISA.

IPR-456 Abrogates uPAR·uPA Binding in Tumor Cells

Immunofluorescence techniques directly visualized the effect of IPR-456 on the uPAR·uPA interaction at the cell surface. Endogenous uPAR and uPA in a breast cancer cell line MDA-MB-231 were immunostained with selective antibodies and visualized by staining with fluorescently-conjugated secondary antibodies. Representative deconvolved confocal immunofluorescence images are presented in Fig. 4a and 4b. To get a quantitative estimate of the effect of IPR-456 on the uPAR and uPA levels we quantified the surface staining intensity for both proteins (Fig. 4c). In cells with clear surface staining, the surface of each cell was outlined using uPAR staining. The pixel immunodensities for uPAR and uPA then were determined using Nikon elements software. In the absence of compound (0.1% DMSO; vehicle control) both uPAR and uPA were detected in large intracellular clusters as well as on surface membranes of the MDA-MB-231 cells (Fig. 4a and 4b). In the presence IPR-456, added 30 min prior to immunostaining, there was a significant concentration-dependent reduction of uPA staining at the cell surface (Fig. 4c) in both cell types. In contrast, there was no change in the immunostaining pattern of uPAR with the DMSO control (Fig. 4c), as expected since uPAR is tethered to the cell surface through a GPI anchor, while uPA is soluble. These results suggest that IPR-456's action was not via a non-specific down-regulation of uPAR, but rather by preventing uPA from binding to uPAR, supporting results from our biochemical assays that IPR-456 acts as a direct inhibitor of the protein-protein interaction.

IPR-456 Blocks Invasion and Migration in a Process Independent of Cell Cytotoxicity

The fact that IPR-456 specifically inhibited uPA binding to uPAR both in recombinant protein assays and at the cell surface of MDA-MB-231 prompted us to test its effects on processes critical for metastasis, including invasion, migration and adhesion. A Boyden chamber apparatus was used to assess the effect of IPR-456 and IPR-803 on MDA-MB-231 invasion. A concentration-dependent reduction in the number of cells that are able to invade through the membrane was observed for both compounds (Fig. 5a). To ensure that the observed inhibition of invasion was not due to cell killing, the level of toxicity of the compounds was measured at each concentration within the timeframe of the invasion experiment (Fig. 5b). Interestingly, IPR-456 showed no toxicity up to 100 μM and minimal toxicity at 200 μM, confirming that the inhibition of invasion is not due to cell killing. IPR-803, on the other hand, showed a concentration dependent inhibition of MDA-MB-231 cell proliferation (Fig. 5b). Photographs of the membrane illustrate the effect of the compound on invasion (Fig. 5c).

To confirm that the effects on invasion observed for IPR-456 are due to targeting of uPAR, knockdown of the receptor using small interfering RNA (siRNA) was performed and confirmed by Western blot analysis (Fig. 5d). Significant impairment of invasion by about 60% in MDA-MB-231 cells is observed for MDA-MB-231 cells lacking uPAR (Fig. 5e). This result confirms what has been widely known, namely that uPAR plays a critical role in invasion. IPR-456 showed no effect on invasion of MDA-MB-231 cells lacking uPAR, confirming that the observed inhibition of invasion by IPR-456 is likely mediated through blocking interactions of uPAR. It is also interesting to note that addition of IPR-456 results in the same effect that was observed with siRNA knockdown of uPAR, namely inhibition of invasion by about 60% (Fig. 5a). Considering 60% as the maximum inhibition that can be achieved by blocking interactions of uPAR, one can estimate an IC_{50} for inhibition of invasion of 30 μM, which is comparable to the 10 μM observed in binding studies by ELISA, SPR and immunofluorescence.

While it has been suggested that interaction of uPAR with integrin promotes cell migration, the role of the uPAR·uPA interaction in this process is not well established. IPR-456

provides an opportunity to dissect the role of this interaction in cancer cell migration. Two different methods were employed. First, a Boyden chamber apparatus was used to assess the effect of compound on chemotaxis based migration. As shown in Fig. 6a and 6b, IPR-456 blocked migration very weakly with an estimated IC_{50} greater than 100 μM. Second, we used a wound healing assay (Fig. 6a and 6b), which assays migration mediated by a concentration gradient established by the wound. This latter assay is not as sensitive to potential cytotoxic effects. As in experiments with the Boyden chamber, IPR-456 showed little effect on migration. Neither assay exhibited any cell cytotoxicity.

As cell adhesion requires integrins, we also tested the role of IPR-456 in MDA-MB-231 cell adhesion. Adherence of cancer cells to fibronectin- or vitronectin-coated microtiter plates was monitored with fluorescence. IPR-456 showed no effect on cell adhesion for MDA-MB-231 cancer cell lines (Fig. 6c). The lack of inhibition was found both on fibronectin- and vitronectin-coated wells.

DISCUSSION

A rational strategy was used to identify small molecules that inhibit the tight uPAR·uPA protein-protein interaction. This strategy consisted of (i) targeting alternative conformational states of uPAR that are distinct from its native crystal structure, and (ii) focusing the docking effort on the binding cavity within uPAR that contains previously-identified hot-spot residues (19). The first component of the strategy was inspired by the conformational selection model of binding for protein-protein interactions (51). In this mechanism, the ligand will "select" the most suitable conformation of the receptor from a pre-existing equilibrium of structures and shift the equilibrium to favor this structure. It was our expectation that the binding of a compound to conformations that were different than the uPAR structure found in the uPAR·uPA complex would further contribute to inhibiting the protein-protein interaction. Docking of a large number of compounds to conformers collected from molecular dynamics simulations led to a small molecule (IPR-456) that binds to uPAR at sub-micromolar affinity with a dissociation equilibrium constant (K_D) of 310 nM. IPR-456 and its derivative IPR-803 displaced GFD-FAM binding, but also inhibited the full protein interaction in a microtiter-based ELISA and surface plasmon resonance with IC_{50} of 10 μM. It is interesting to note that compounds that emerged from virtual screening of the crystal structure showed little overlap with those that emerged from the multi-conformer docking (Table S1 in Supporting Information). Only one compound, namely IPR-576, appeared in both lists and the compound was shown not to bind to uPAR in our FP assay.

Free energy calculations provided insight into the binding mechanism of IPR-456 to contrast with IPR-566 and IPR-593, which bind to uPAR and displace GFD-FAM, but do not inhibit the full protein interaction. The calculations revealed that IPR-456 engaged more hot-spot residues than the other two compounds, made stronger interactions with the residues within the binding site, and showed significant affinity to a charged residue, namely Arg53. Interestingly, the strong interaction of IPR-456 to Arg53 was reminiscent of the native peptide GFD that also exhibited preferred binding with the residue. Visualizations of the uPAR/IPR-456 trajectories suggested that the carboxylate moiety on IPR-456 was likely the basis for the strong interaction of the compound with Arg53. This hypothesis was confirmed by testing the *in vitro* activity of a series of derivatives that lacked the carboxylate of the parent compound. The results showed complete loss of inhibition of the protein-protein interaction in the absence of the carboxylate. The precise position of the carboxylate on the phenyl ring did not appear to impair activity, but the negative charge of the carboxylate was the more critical component for inhibition. In fact, mere conversion of the carboxylate to a methyl ester derivative led to complete loss of activity. The critical nature of this

carboxylate moiety could serve as a general mechanism for transforming molecules that merely bind to a target in a protein-protein interaction, to molecules that fully inhibit the interaction, by simply introducing a charged group to engage nearby charged residues.

Highly invasive breast MDA-MB-231 tumor cells are known to overexpress uPAR. We showed that IPR-456 specifically blocked the uPAR·uPA interaction using immunofluorescence imaging in MDA-MB-231 cells, which employs antibodies labeled with fluorescent probes specific to uPAR and uPA. The results indicated that IPR-456 significantly impaired presence of uPA at the cell surface, but had no effect on the uPAR levels. The lack of effect on the levels of uPAR at the cell surface confirms that the compound is unlikely to be acting through some non-specific mechanism by down-regulating the receptor, but more likely via a direct block of the interaction.

Compound IPR-456 offers a chemical tool to disentangle the role of the uPAR·uPA from other interactions of uPAR and study its role in metastasis. IPR-456 inhibits MDA-MB-231 invasion with an IC_{50} of approximately 30 μM. This IC_{50} is comparable to the 10 μM IC_{50} observed for inhibition of uPA_{ATF} binding to uPAR in the ELISA and SPR competitive assays. The three-fold discrepancy may be attributed to the fact that uPAR promotes invasion through other interactions with other cell surface receptors. IPR-456 also provided a unique opportunity to probe the role of the uPAR·uPA interaction in other processes that promote metastasis, such as migration and adhesion. Interestingly, the compound did not show significant effect on migration in two different assays and had no effect on adhesion. The lack of effect on adhesion suggests that the interaction likely is not involved in binding and activating $\alpha_5\beta_1$ and $\alpha_3\beta_1$ integrins (52, 53). These results indicate that uPAR is likely to engage integrins through alternative sites on the receptor, perhaps at the vitronectin binding site located away from the uPA binding site (52–54). IPR-803 exhibited some cytotoxicity compared with IPR-456. There is a possibility that this is due to intracellular off-targets. The different position of the carboxylate on IPR-803 perhaps facilitates its transport into cells through any of the different cellular transport mechanisms, enabling the compound to reach potential intracellular off-targets.

The discovery of IPR-456 suggests that virtual screening targeting alternative conformations sampled from molecular dynamics simulations is a viable approach to identify small molecules that inhibit challenging protein-protein interactions. IPR-456 and its derivatives provide powerful chemical probes to delineate the role of the uPAR·uPA interaction in various processes in metastasis. These compounds have the potential to serve as leads for the development of *in vivo* chemical probes and therapeutics to block metastasis.

Supplementary Material

Refer to Web version on PubMed Central for supplementary material.

Acknowledgments

References

1. Shapiro RL, Duquette JG, Nunes I, Roses DF, Harris MN, Wilson EL, Rifkin DB. Urokinase-type plasminogen activator-deficient mice are predisposed to staphylococcal botryomycosis, pleuritis, and effacement of lymphoid follicles. The American journal of pathology. 1997; 150:359–369. [PubMed: 9006351]

2. Gandhari M, Arens N, Majety M, Dorn-Beineke A, Hildenbrand R. Urokinase-type plasminogen activator induces proliferation in breast cancer cells. International Journal of Oncology. 2006; 28:1463–1470. [PubMed: 16685447]

3. Liang X, Yang X, Tang Y, Zhou H, Liu X, Xiao L, Gao J, Mao Z. RNAi-mediated downregulation of urokinase plasminogen activator receptor inhibits proliferation, adhesion, migration and invasion in oral cancer cells. Oral Oncol. 2008

4. Kondraganti S, Gondi CS, McCutcheon I, Dinh DH, Gujrati M, Rao JS, Olivero WC. RNAi-mediated downregulation of urokinase plasminogen activator and its receptor in human meningioma cells inhibits tumor invasion and growth. Int J Oncol. 2006; 28:1353–1360. [PubMed: 16685436]

5. Prager GW, Breuss JM, Steurer S, Olcaydu D, Mihaly J, Brunner PM, Stockinger H, Binder BR. Vascular endothelial growth factor receptor-2-induced initial endothelial cell migration depends on the presence of the urokinase receptor. Circ Res. 2004; 94:1562–1570. [PubMed: 15131009]

6. Schiller HB, Szekeres A, Binder BR, Stockinger H, Leksa V. Mannose 6-phosphate/insulin-like growth factor 2 receptor limits cell invasion by controlling alphaVbeta3 integrin expression and proteolytic processing of urokinase-type plasminogen activator receptor. Molecular biology of the cell. 2009; 20:745–756. [PubMed: 19037107]

7. Andreasen PA, Kjoller L, Christensen L, Duffy MJ. The urokinase-type plasminogen activator system in cancer metastasis: A review. Int J Cancer. 1997; 72:1–22. [PubMed: 9212216]

8. Mignatti P, Rifkin DB. Plasminogen activators and matrix metalloproteinases in angiogenesis. Enzyme & protein. 1996; 49:117–137. [PubMed: 8797002]

9. Rabbani SA, Mazar AP. The role of the plasminogen activation system in angiogenesis and metastasis. Surgical oncology clinics of North America. 2001; 10:393–415. x. [PubMed: 11382594]

10. Subramanian R, Gondi CS, Lakka SS, Jutla A, Rao JS. siRNA-mediated simultaneous downregulation of uPA and its receptor inhibits angiogenesis and invasiveness triggering apoptosis in breast cancer cells. International Journal of Oncology. 2006; 28:831–839. [PubMed: 16525631]

11. Kunigal S, Lakka SS, Gondi CS, Estes N, Rao JS. RNAi-mediated downregulation of urokinase plasminogen activator receptor and matrix metalloprotease-9 in human breast cancer cells results in decreased tumor invasion, angiogenesis and growth. International journal of cancer. 2007; 121:2307–2316.

12. Wei Y, Lukashev M, Simon DI, Bodary SC, Rosenberg S, Doyle MV, Chapman HA. Regulation of integrin function by the urokinase receptor. Science. 1996; 273:1551–1555. [PubMed: 8703217]

13. Kiyan J, Kiyan R, Haller H, Dumler I. Urokinase-induced signaling in human vascular smooth muscle cells is mediated by PDGFR-beta. Embo J. 2005; 24:1787–1797. [PubMed: 15889147]

14. Liu D, Aguirre Ghiso J, Estrada Y, Ossowski L. EGFR is a transducer of the urokinase receptor initiated signal that is required for in vivo growth of a human carcinoma. Cancer cell. 2002; 1:445–457. [PubMed: 12124174]

15. Resnati M, Pallavicini I, Wang JM, Oppenheim J, Serhan CN, Romano M, Blasi F. The fibrinolytic receptor for urokinase activates the G protein-coupled chemotactic receptor FPRL1/LXA4R. P Natl Acad Sci USA. 2002; 99:1359–1364.

16. Mazar AP. Urokinase plasminogen activator receptor choreographs multiple ligand interactions: implications for tumor progression and therapy. Clin Cancer Res. 2008; 14:5649–5655. [PubMed: 18794071]

17. Arkin MR, Wells JA. Small-molecule inhibitors of protein-protein interactions: progressing towards the dream. Nature reviews. 2004; 3:301–317.

18. Ploug M, Ellis V. Structure-function relationships in the receptor for urokinase-type plasminogen activator. Comparison to other members of the Ly-6 family and snake venom alpha-neurotoxins. Febs Lett. 1994; 349:163–168. [PubMed: 8050560]

19. Gardsvoll H, Gilquin B, Le Du MH, Menez A, Jorgensen TJ, Ploug M. Characterization of the functional epitope on the urokinase receptor. Complete alanine scanning mutagenesis supplemented by chemical cross-linking. The Journal of biological chemistry. 2006; 281:19260–19272. [PubMed: 16672229]

20. Huai Q, Mazar AP, Kuo A, Parry GC, Shaw DE, Callahan J, Li YD, Yuan C, Bian CB, Chen LQ, Furie B, Furie BC, Cines DB, Huang MD. Structure of human urokinase plasminogen activator in complex with its receptor. Science. 2006; 311:656–659. [PubMed: 16456079]

21. Wells JA, McClendon CL. Reaching for high-hanging fruit in drug discovery at protein-protein interfaces. Nature. 2007; 450:1001–1009. [PubMed: 18075579]

22. Christ F, Voet A, Marchand A, Nicolet S, Desimmie BA, Marchand D, Bardiot D, Van der Veken NJ, Van Remoortel B, Strelkov SV, De Maeyer M, Chaltin P, Debyser Z. Rational design of small-molecule inhibitors of the LEDGF/p75-integrase interaction and HIV replication. Nature Chemical Biology. 2010; 6:442–448.

23. Cerchietti LC, Ghetu AF, Zhu X, Da Silva GF, Zhong SJ, Matthews M, Bunting KL, Polo JM, Fares C, Arrowsmith CH, Yang SN, Garcia M, Coop A, MacKerell AD, Prive GG, Melnick A. A Small-Molecule Inhibitor of BCL6 Kills DLBCL Cells In Vitro and In Vivo. Cancer cell. 2010; 17:400–411. [PubMed: 20385364]

24. Oltersdorf T, Elmore SW, Shoemaker AR, Armstrong RC, Augeri DJ, Belli BA, Bruncko M, Deckwerth TL, Dinges J, Hajduk PJ, Joseph MK, Kitada S, Korsmeyer SJ, Kunzer AR, Letai A, Li C, Mitten MJ, Nettesheim DG, Ng S, Nimmer PM, O'Connor JM, Oleksijew A, Petros AM, Reed JC, Shen W, Tahir SK, Thompson CB, Tomaselli KJ, Wang B, Wendt MD, Zhang H, Fesik SW, Rosenberg SH. An inhibitor of Bcl-2 family proteins induces regression of solid tumours. Nature. 2005; 435:677–681. [PubMed: 15902208]

25. He MM, Smith AS, Oslob JD, Flanagan WM, Braisted AC, Whitty A, Cancilla MT, Wang J, Lugovskoy AA, Yoburn JC, Fung AD, Farrington G, Eldredge JK, Day ES, Cruz LA, Cachero TG, Miller SK, Friedman JE, Choong IC, Cunningham BC. Small-molecule inhibition of TNF-alpha. Science. 2005; 310:1022–1025. [PubMed: 16284179]

26. Vassilev LT, Vu BT, Graves B, Carvajal D, Podlaski F, Filipovic Z, Kong N, Kammlott U, Lukacs C, Klein C, Fotouhi N, Liu EA. In vivo activation of the p53 pathway by small-molecule antagonists of MDM2. Science. 2004; 303:844–848. [PubMed: 14704432]

27. Roehrl MH, Kang S, Aramburu J, Wagner G, Rao A, Hogan PG. Selective inhibition of calcineurin-NFAT signaling by blocking protein-protein interaction with small organic molecules. Proceedings of the National Academy of Sciences of the United States of America. 2004; 101:7554–7559. [PubMed: 15131267]

28. Keskin Z, Gursoy A, Ma B, Nussinov R. Principles of protein-protein interactions: What are the preferred ways for proteins to interact? Chem Rev. 2008; 108:1225–1244. [PubMed: 18355092]

29. Bruncko M, Oost TK, Belli BA, Ding H, Joseph MK, Kunzer A, Martineau D, McClellan WJ, Mitten M, Ng SC, Nimmer PM, Oltersdorf T, Park CM, Petros AM, Shoemaker AR, Song X, Wang X, Wendt MD, Zhang H, Fesik SW, Rosenberg SH, Elmore SW. Studies leading to potent, dual inhibitors of Bcl-2 and Bcl-xL. Journal of medicinal chemistry. 2007; 50:641–662. [PubMed: 17256834]

30. Totrov M, Abagyan R. Flexible ligand docking to multiple receptor conformations: a practical alternative. Curr Opin Struct Biol. 2008; 18:178–184. [PubMed: 18302984]

31. Gardsvoll H, Hansen LV, Jorgensen TJ, Ploug M. A new tagging system for production of recombinant proteins in Drosophila S2 cells using the third domain of the urokinase receptor. Protein expression and purification. 2007; 52:384–394. [PubMed: 17215141]

32. Kunapuli P, Chitta KS, Cowell JK. Suppression of the cell proliferation and invasion phenotypes in glioma cells by the LGI1 gene. Oncogene. 2003; 22:3985–3991. [PubMed: 12821932]

33. Word JM, Lovell SC, Richardson JS, Richardson DC. Asparagine and glutamine: using hydrogen atom contacts in the choice of side-chain amide orientation. Journal of molecular biology. 1999; 285:1735–1747. [PubMed: 9917408]

34. Sanner MF. Python: A programming language for software integration and development. Journal of Molecular Graphics & Modelling. 1999; 17:57–61. [PubMed: 10660911]

35. Morris GM, Goodsell DS, Halliday RS, Huey R, Hart WE, Belew RK, Olson AJ. Automated docking using a Lamarckian genetic algorithm and an empirical binding free energy function. J Comp Chem. 1998; 19:1639–1662.

36. Irwin JJ, Shoichet BK. ZINC - A free database of commercially available compounds for virtual screening. J Chem Inf Model. 2005; 45:177–182. [PubMed: 15667143]

37. Jorgensen WL, Chandrasekhar J, Madura JD, Impey RW, Klein M. Comparison of simple potential functions for simulating liquid water. The Journal of Chemical Physics. 1983; 79:10.

38. Case, DA.; Cheatham, TADTE., III; Simmerling, CL.; Wang, J.; Duke, RE.; Luo, R.; Merz, KM.; Wang, B.; Pearlman, DA.; Crowley, M.; Brozell, S.; Tsui, V.; Gohlke, H.; Mongan, J.; Hornak, V.; Cui, G.; Beroza, P.; Schafmeister, C.; Caldwell, JW.; Ross, WS.; Kollman, PA. AMBER 8. University of California; San Francisco: 2004.

39. Li L, Uversky VN, Dunker AK, Meroueh SO. A computational investigation of allostery in the catabolite activator protein. Journal of the American Chemical Society. 2007; 129:15668–15676. [PubMed: 18041838]

40. Chong LT, Dempster SE, Hendsch ZS, Lee LP, Tidor B. Computation of electrostatic complements to proteins: a case of charge stabilized binding. Protein Sci. 1998; 7:206–210. [PubMed: 9514276]

41. Jakalian A, Jack DB, Bayly BI. Fast, efficient generation of high-quality atomic charges. AM1-BCC model: II. Parameterization and Validation. J Comput Chem. 2002; 23:18.

42. Gohlke H, Kiel C, Case DA. Insights into protein-protein binding by binding free energy calculation and free energy decomposition for the Ras-Raf and Ras-RalGDS complexes. Journal of molecular biology. 2003; 330:891–913. [PubMed: 12850155]

43. Gornostaev LA, DoIgushina LV, Titova NG, Arnol'd EV, Lavrikova TI. Synthesis of 3-alkyl-5-arylamino-6,11-dihydro-3H-anthra[1,2-d]-[1,2,3]triazole-6,11-dione 2-oxides by nitrosation of 3-alkyl-amino-5-arylamino-6H-anthra[1,9-cd]isoxazol-6-ones. Russ J Org Chem+. 2006; 42:1364–1367.

44. Brittain JM, Piekarz AD, Wang Y, Kondo T, Cummins TR, Khanna R. An atypical role for collapsin response mediator protein 2 (CRMP-2) in neurotransmitter release via interaction with presynaptic voltage-gated calcium channels. The Journal of biological chemistry. 2009; 284:31375–31390. [PubMed: 19755421]

45. Feng BY, Shoichet BK. A detergent-based assay for the detection of promiscuous inhibitors. Nat Protoc. 2006; 1:550–553. [PubMed: 17191086]

46. Liang S, Li L, Hsu WL, Pilcher MN, Uversky V, Zhou Y, Dunker AK, Meroueh SO. Exploring the molecular design of protein interaction sites with molecular dynamics simulations and free energy calculations. Biochemistry. 2009; 48:399–414. [PubMed: 19113835]

47. Li L, Liang S, Pilcher MM, Meroueh SO. Incorporating receptor flexibility in the molecular design of protein interfaces. Protein Engineering Design and Selection. 2009; 22:575–586.

48. Li L, Uversky VN, Dunker AK, Meroueh SO. A computational investigation of allostery in the catabolite activator protein. Journal of the American Chemical Society. 2007; 129:15668–15676. [PubMed: 18041838]

49. Gardsvoll H, Werner F, Sondergaard L, Dano K, Ploug M. Characterization of low-glycosylated forms of soluble human urokinase receptor expressed in Drosophila Schneider 2 cells after deletion of glycosylation-sites. Protein expression and purification. 2004; 34:284–295. [PubMed: 15003263]

50. Niesen FH, Berglund H, Vedadi M. The use of differential scanning fluorimetry to detect ligand interactions that promote protein stability. Nature Protocols. 2007; 2:2212–2221.

51. Boehr DD, Nussinov R, Wright PE. The role of dynamic conformational ensembles in biomolecular recognition. Nature Chemical Biology. 2009; 5:789–796.

52. Wei Y, Czekay RP, Robillard L, Kugler MC, Zhang F, Kim KK, Xiong JP, Humphries MJ, Chapman HA. Regulation of alpha5beta1 integrin conformation and function by urokinase receptor binding. J Cell Biol. 2005; 168:501–511. [PubMed: 15684035]

53. Wei Y, Eble JA, Wang ZM, Kreidberg JA, Chapman HA. Urokinase receptors promote beta 1 integrin function through interactions with integrin alpha 3 beta 1. Molecular biology of the cell. 2001; 12:2975–2986. [PubMed: 11598185]

54. Gardsvoll H, Ploug M. Mapping of the vitronectin-binding site on the urokinase receptor: involvement of a coherent receptor interface consisting of residues from both domain I and the flanking interdomain linker region. The Journal of biological chemistry. 2007; 282:13561–13572. [PubMed: 17355965]
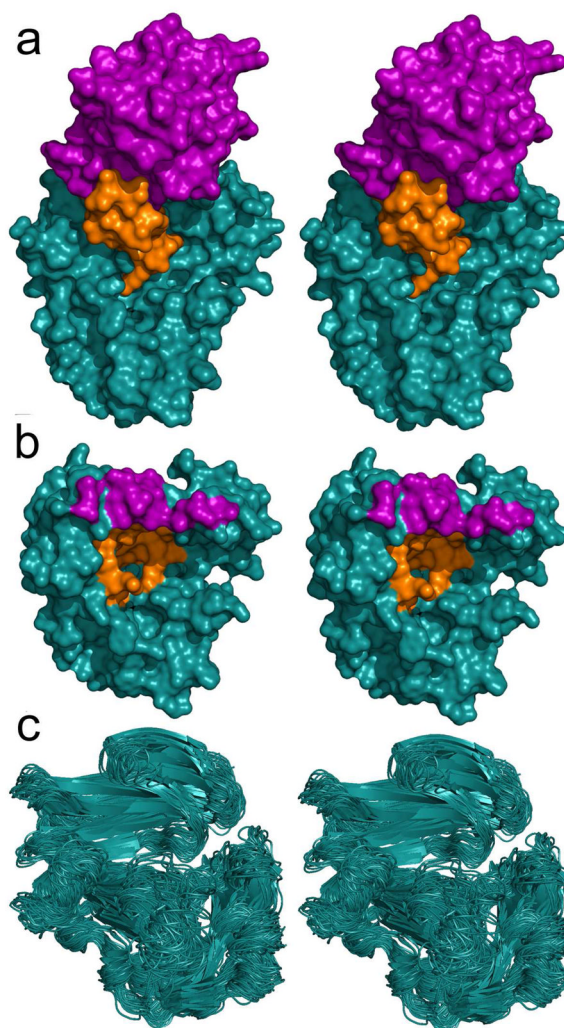
Figure 1. Three dimensional structure of uPAR in complex with its binding partners
(a) Stereo view of the three-dimensional structure of the complex between uPAR, uPA$_{ATF}$.
A solvent-accessible surface is constructed around each protein. uPAR is shown in cyan,
uPA$_{ATF}$ is shown in purple and orange, and the growth factor-like domain (GFD) within
uPA$_{ATF}$ is shown in orange. (b) Stereo view of uPAR in surface representation with the uPA
interaction surface is shown for GFD (orange), uPA$_{ATF}$ (purple), and cyan (rest of protein).
(c) Stereo view of the superimposition of the 50 conformers that were used during the virtual
screening that led to active compounds.
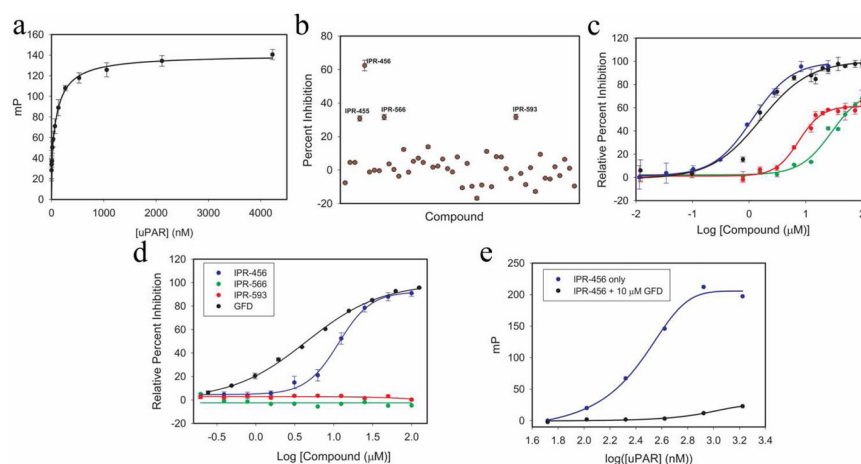
Figure 2. IPR-456 Inhibits uPA binding to uPAR
(a) Binding of fluorescent GFD (GFD-FAM) as a function of uPAR. Increasing concentration of suPAR protein were titrated against the fluorescent GFD-FAM peptide and data was fit to a sigmoidal dose-dependent curve to determine a K_d of 0.120 μM. **(b)** Fluorescence polarization for the 50 compounds that emerged from the computational screening **(c)** Displacement of GFD-FAM from uPAR by GFD-FAM (black curve) and three compounds, namely IPR-456, IPR-566, and IPR-593, that exhibited dose-dependent inhibition (blue, green and red curves); **(d)** An ELISA was used to measure inhibition of uPAR binding to uPA$_{ATF}$-coated microtiter plate by serial dilutions of compounds **(e)** Fluorescence polarization (mP) for IPR456 measured at emission of 600 nm with increasing concentration of uPAR is shown; competition by the addition of 10 μM GFD to the titration of IPR456 with uPAR is also shown (black curve). The estimated dissociation constant (K_d) of IPR-456 to uPAR is 140 nM.
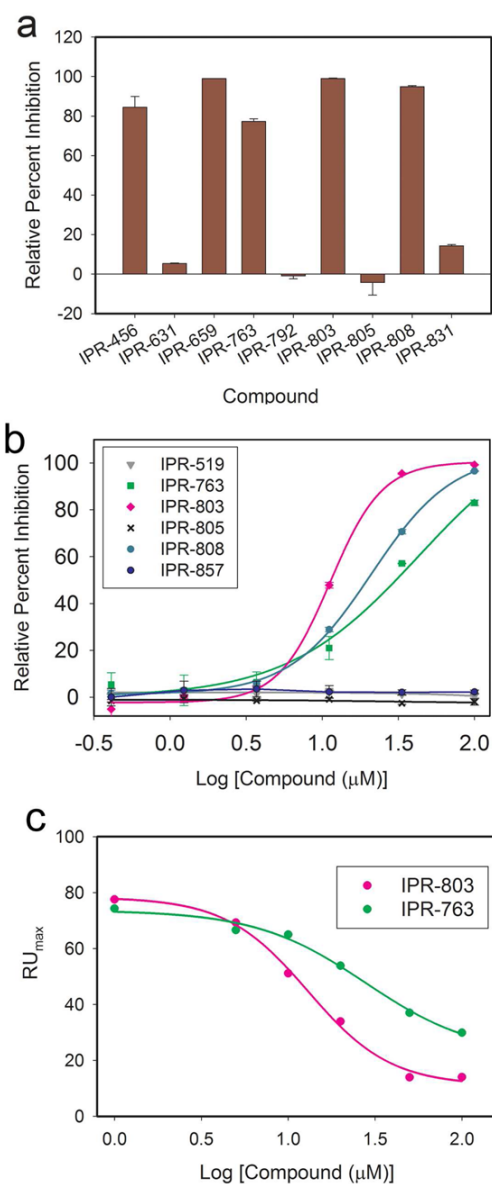
Figure 3. IPR-456 Derivatives Inhibit uPAR·uPA Interaction
(**a**) ELISA for IPR-456 and its derivatives at 50 μM concentration. (**b**) An ELISA was used to measure inhibition of uPAR binding to uPA_{ATF}-coated microtiter plate by serial dilutions of IPR-456 derivatives (IPR-763, IPR-803, IPR-805, and IPR-808). IPR-519 is a negative control to rule out non-specific inhibition due to carboxylic acid. (**c**) A competition assay using surface plasmon resonance (SPR) assay with uPAR injected along with increasing concentration of compound on immobilized uPA.
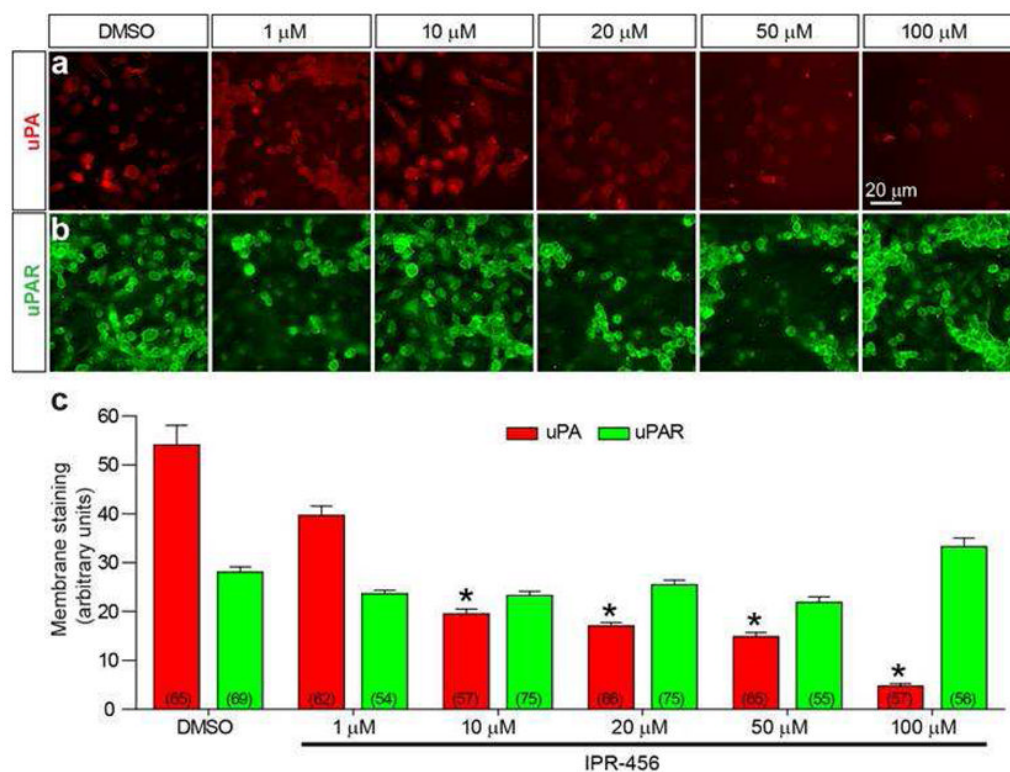
Figure 4. IPR-456 interferes with cell surface uPA binding in breast cancer cells
Representative deconvolved confocal immunofluorescence images of MDA-MB-231 cells
stained with **(a)** a monoclonal antibody against uPAR (green) and **(b)** a polyclonal antibody
against uPA (red). **(c)** Quantification of the surface expression levels of uPA and uPAR in
MDA-MB-231 cells. The plasma membrane outlines were identified with uPAR staining.
The pixel immunodensity of the surface uPA and uPAR was calculated from these regions
only. Only cells where the cell membrane was clearly discernible were included in the
analysis. Each value represents the mean ± S.E. from 26–30 cells taken from three different
fields from two independent samples. * significant difference from the DMSO control ($p <$
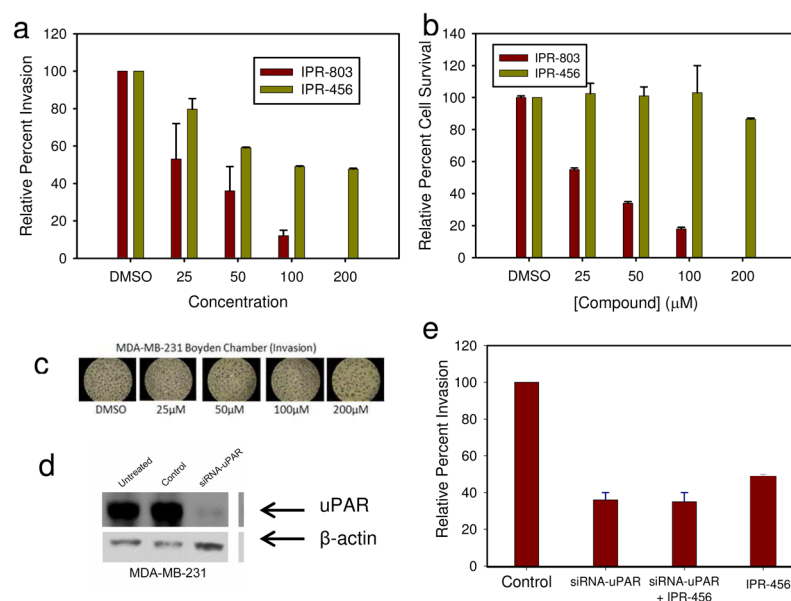0.001, Student's t test).

Figure 5. Compounds block invasion, migration, but not adhesion of breast (MDA-MB-231) cancer cells
(a) Invasion of MDA-MB-231 cells at increasing concentration of IPR-456 and IPR-803, as indicated. Ten fields of unit area on each membrane were counted for cell numbers (magnification, 200×). These data represent the average ± SD of three independent experiments. *$P < 0.05$, paired one-tailed t-test **(b)** Effect of IPR-456 and IPR-803 on MDA-MB-231 cell proliferation. **(c)** Representative experimental cells from control and in the presence of increasing concentration of IPR-456 were photographed for the Boyden chamber assays (200×) to illustrate the effect of IPR-456 on invasion. **(d)** MDA-MB-231 cells were transfected with siRNAs for uPAR, control siRNA (control) or with transfection reagent only (mock). After 48 h, cells were lysed and analysed by immunoblotting. **(e)** Invasion in the absence (control) or with IPR-456 for MDA-MB-231 with siRNA knockdown of uPAR.
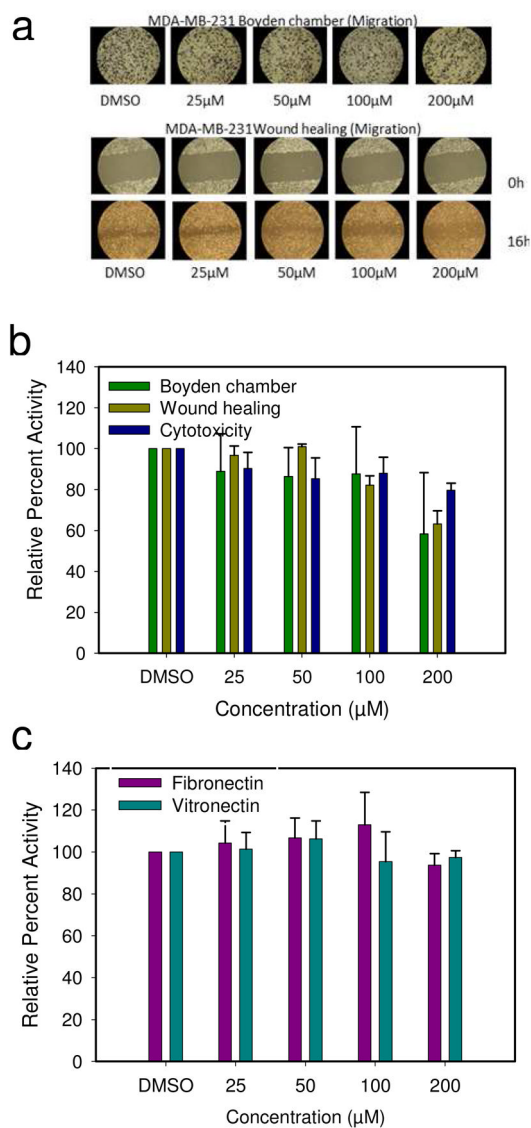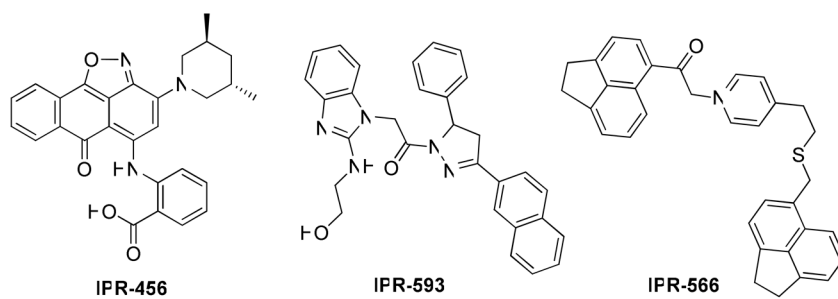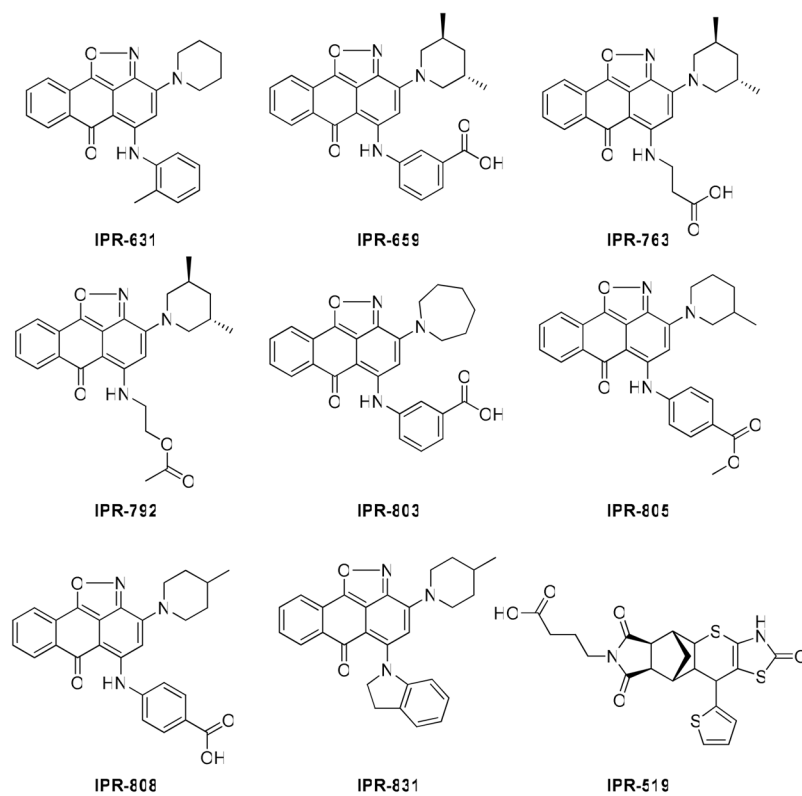
Figure 6. IPR-456 effect on migration and adhesion
(a) Representative experimental cells from control and in the presence of increasing concentration of IPR-456 were photographed for the wound healing (100× magnification) and Boyden chamber assays (200× magnification). **(b)** IPR-456 effect on MDA-MB-231 migration were quantified as described in Methods **(c)** The adhesion of MDAMB231 cells to ECM components fibronectin (FN) or vitronectin (VN) in the absence or presence of IPR-456 are shown as indicated. The numbers of attached cells were quantified by MTT assay.

IPR-456   **IPR-593**   **IPR-566**

SCHEME 1.

IPR-631

IPR-659

IPR-763

IPR-792

IPR-803

IPR-805

IPR-808

IPR-831

IPR-519

SCHEME 2.

Table 1

Binding energy from free energy calculation based on explicit-solvent molecular dynamics simulations.[a]

Compound	ΔE (kcal mol⁻¹)						
IPR-456	Arg53(−5.3)	Leu150(−2.7)	Val125(−1.8)	Leu55(−1.5)	Leu144(−1.2)	Leu168(−1.1)	Ala255(−1.0)
IPR-566	Ala255(−1.8)	Leu168(−1.7)	Val125(−1.4)	Leu150(−1.4)	Ser257(−1.0)		
IPR-593	Leu150(−2.0)	Leu55(−1.8)	Arg53(−1.6)	Leu168(−1.5)	Ala255(−1.4)	Val125(−1.2)	
GFD	Arg53(−2.4)	Thr127(−2.3)	His166(−1.8)	Leu150(−1.7)	Asp254(−1.6)	Asp140(−1.5)	Leu55(−1.5)

[a]Residue-based free energy calculations shown for all residues that interact with IPR-456, IPR-566, IPR-593 and GFD. The interaction energy between the residue (ΔEGBTOT) is shown in parentheses in kcal•mol⁻¹. Only residues with ΔEGBTOT ≤ −1.0 are listed. Residues that exhibited a penalty greater than 0.5 kcal•mol⁻¹ and less than 1 kcal•mol⁻¹ for uPA binding to uPAR from a recent alanine scanning surface plasmon resonance (SPR) study (19) are colored in purple, while residues led to more than 1 kcal•mol⁻¹ loss of affinity for uPA are shown in firebrick red. Residues that did not show any effect on binding of uPA from the SPR study were colored in cyan.